Ceramics International 48 (2022) 353–362

Contents lists available at ScienceDirect

Ceramics International

journal homepage: www.elsevier.com/locate/ceramint

Close-to-ideal spin polarization in zinc-doped Fe–Mo double perovskites at the nanoscale

Le Duc Hien [a,b], Luong Ngoc Anh [a], Phuc Duong Nguyen [a,*], To Thanh Loan [a], Siriwat Soontaranon [c], Dao Thi Thuy Nguyet [a], Ta Van Khoa [b], Anne de Visser [d]

[a] International Training Institute for Materials Science (ITIMS), Hanoi University of Science and Technology, Hanoi, 10000, Viet Nam
[b] Technology Institute – General Department of Defense Technology, Duc Thang, North Tu Lien, Hanoi, 10000, Viet Nam
[c] Synchrotron Light Research Institute, University Avenue 111, Nakhon Ratchasima, 30000, Thailand
[d] Van der Waals–Zeeman Institute, University of Amsterdam, Science Park 904, NL-1098, XH, Amsterdam, the Netherlands

ARTICLE INFO

Keywords:
Nano-sized $Sr_2Fe_{1-x}Zn_xMoO_6$
Cationic order
Superparamagnetism
Magnetization
Magnetoresistance
Spin polarization

ABSTRACT

A high degree of spin polarization in half-metallic double perovskites is a prerequisite for several applications in spintronics, which depends crucially on the cationic order of the systems. This paper reports a study on tailoring the structure and morphology of nano-sized $Sr_2Fe_{1-x}Zn_xMoO_6$ ($x = 0.05$, 0.1, 0.15) materials to improve their spin polarization. The combined analysis of synchrotron X-ray diffraction and magnetization data shows that Zn replaces Fe in the B sites. Although the majority of particles have lateral dimensions in the range 30–60 nm as observed by scanning electron microscope, the samples with $x = 0.1$ and 0.15 show finite-size effects with superparamagnetism below room temperature and a reduced Curie temperature (from 410 K for $x = 0.05$–390 K for $x = 0.15$). The results are due to the formation of networks of insulating Mo–O–Zn–O–Mo linkages and anti-phase boundaries, which divide the particles into smaller domains with a mean diameter of ~11 nm as determined via a Langevin fit. The almost perfectly ordered structure in the nanodomains is responsible for a high magnetoresistance ratio. A value of -42% at 5 K in 50 kOe is recorded for the sample $x = 0.15$. Via fitting the magnetoresistance curve using the Inoue-Mekagawa theory, the spin polarization of 99% is determined.

1. Introduction

The Fe–Mo-based double perovskites have a general formula A_2FeMoO_6 in which the FeO_6 and MoO_6 octahedra accommodate in two stacked FCC sublattices [1–3]. The A sites can take 2+ valence ions (earth alkalines) or 3+ valence ions (rare earths, lead, or bismuth). In an ideal structure, the alternating FeO_6 and MoO_6 octahedra form B and B' sublattices, respectively. The strong antiferromagnetic exchange interaction between the magnetic Fe^{3+} and Mo^{5+} ions leads to a ferrimagnetic structure [1,4]. These materials have sizable net magnetization and magnetic ordering temperature (T_C) above room temperature. Hence, they are promising for device applications using magnetoresistive (MR) [4–7], magnetocaloric (MCE) [8–10] and magnetoelectric (ME) effects [3,11,12]. In practice, a certain amount of Fe often locates on the B' sites and vice versa, which is known as anti-site disorders. This unwanted effect leads to the loss of the net magnetization, T_C value, spin polarization, ferroelectric polarization, and the broadening of the magnetic phase transition [13–17]. To obtain samples with highly ordered structure, different preparation techniques were employed such as floating-zone [18,19], solid-state reaction [20,21], epitaxial growth [22], sputtering [23], and wet-chemical methods [24,25].

We have systematically studied the influence of heat treatment conditions on the phase formation and cationic order of the Sr_2FeMoO_6 (SFMO) particles obtained via the sol-gel process [16,26]. The sample obtained after annealing the gel precursor at 1200 °C for 8 h in an argon atmosphere mixed with 15 vol % H_2 has the highest cationic order of 90%. The magnetization of the sample is reduced compared to the theoretical value of the perfectly ordered structure. However, the spin polarization at 5 K derived from the analysis of the magnetoresistance data is considerably higher than expected from electronic structure calculations by assuming a homogenous distribution of anti-site defects in the lattice [16]. Our finding indicated that the nature of the structural disorder plays a decisive role in the spin-dependent electrical conduction of the system. Via analyzing X-ray diffraction and X-ray absorption fine structure (XAFS) data for polycrystalline Sr_2FeMoO_6 samples, Meneghini et al. showed that a high degree of short-range order is

* Corresponding author.
E-mail addresses: duong@itims.edu.vn, duong.nguyenphuc@hust.edu.vn (P.D. Nguyen).

https://doi.org/10.1016/j.ceramint.2021.09.110
Received 22 June 2021; Received in revised form 18 August 2021; Accepted 9 September 2021
Available online 12 September 2021

preserved even in samples with highly reduced long-range chemical order [27]. Their results imply that the anti-site defects in practice are not distributed homogeneously but rather segregate together to form patches of nanometer dimensions. These short patches connect to the original lattice via the anti-phase boundaries (APBs), e.g., the Fe–O–Fe links. The same situation may hold for our samples where segregation of anti-site defects leaves the matrix phase closer to the ideal atomic structure. Therefore, the spin polarization remains high. On the other hand, the anti-phase structural domains at the nanoscale influence the magnetization process and the local alignment of spins. Evidence of a disorder-induced magnetic spin-glass phase and superparamagnetic behavior in Sr_2FeMoO_6 nanosized grains was shown by several groups [28–30].

Previous works showed that substituting small amounts of other metal elements for Fe such as Mn, Ni, Mg, and Zn improves the cationic order in the SFMO structure [31–37]. Mn and Mg dopants deteriorate the Curie temperature T_C, saturation magnetization M_s, and magnetoresistance MR [31,32,35]. On the contrary, doping Ni leads to an increase of T_C and M_s [33]. Wang et al. reported that in the $Sr_2Fe_{1-x}Zn_xMoO_6$ bulk samples ($0 \leq x \leq 0.2$), Zn^{2+} ions partially replace Fe^{3+} at the B' sites. Thereby, the number of antiferromagnetic Fe–O–Fe pairs decreases, and non-magnetic and insulating Mo–O–Zn–O–Mo chains form. These insulating chains can act as potential barriers for electron tunneling processes and divide the lattice into small ferromagnetic regions [36]. The latter can be magnetized easily, and therefore the low-field magnetoresistance of the samples is enhanced. The results show that adding small amounts of appropriate metal elements in the Fe–Mo double perovskites results in a higher degree of cationic order, and the physical properties are improved. However, so far, optimization of magnetoresistance in doped SFMO materials has not been fully implemented, and information on the influence of doping elements on cationic order and spin polarization is still limited. In addition, understanding the finite-size effects on the magnetic properties of the systems at the nanoscale needs further investigation.

In this paper, we prepared the particle systems with nominal composition $Sr_2Fe_{1-x}Zn_xMoO_6$ (SFZMO) and investigated their cation distribution, microstructure, magnetic and electrical properties. Superparamagnetic behavior and the tunneling magnetoresistance mechanism were clarified. Spin polarization of nearly 100% was found for the composition $x = 0.15$.

2. Experiments

2.1. Sample preparation

SFZMO particle systems were prepared by using the sol-gel method. Details of the procedure were described elsewhere [16]. Starting materials are nitrate salts of Sr^{2+}, Fe^{3+}, and Zn^{2+}, and $(NH_4)_6Mo_7O_{24}$. Chemicals used were of analytical grade and were provided by Sigma-Aldrich. Solutions of $Fe(NO_3)_3$, $Sr(NO_3)_2$, and $Zn(NO_3)_2$ were mixed with citric acid ($C_6H_8O_7$). The aqueous mixture was then added to a solution of $(NH_4)_6Mo_7O_{24}$. The molar ratios of the metal ions are set according to the chemical formula of $Sr_2Fe_{1-x}Zn_xMoO_6$ with $x = 0$, 0.05, 0.1, and 0.15. The molar amount of citric acid is about three times larger than the total amount of the metal ions. The final solution was stirred vigorously at 80 °C until a gel state was achieved. The gel was dried at 110 °C for 24 h, then ground and heated at 500 °C for 2 h. The intermediate powders were pressed into pellets under a pressure of 2.5 tons/cm^2 and subsequently annealed under a stream of H_2/Ar mixed gas (15 vol% H_2) with a flow rate of 10 sccm at 1200 °C for 8 h to form the crystallized samples. The temperature in the furnace was ramped from room temperature to 1200 °C in about 40 min. The chemical composition of the final products was monitored by using an inductively coupled plasma atomic emission spectroscopy (ICP-AES, Thermo Fisher Scientific ICP-IRIS). During the preparation, the amounts of the starting salts were adjusted, and the whole process was repeated to obtain the samples with compositions close to the nominal atomic ratios.

2.2. Measuring techniques

The crystal structure was studied using synchrotron X-ray powder diffraction (SXRD), which was done at the beamline Small/Wide Angle X-ray Scattering (SAXS/WAXS) of the Synchrotron Light Research Institute (Thailand) (wavelength $\lambda = 1.54$ Å). The structural parameters were determined via Rietveld analysis using the FullProf program [38]. A pseudo-Voigt function was used to fit the diffraction peaks. Instrumental artifacts were corrected by using a LaB_6 standard. The refinement quality was checked by the goodness (χ^2) and the weighted profile R-factor (R_{wp}) [39].

The morphology and the grain size distribution were studied using a Field Emission-Scanning Electron Microscopy (FESEM) (JEOL JSM–7600F).

The magnetization was measured using a vibrating sample magnetometer (VSM) in a PPMS DynaCool system. The measurements were carried out in the temperature region 5–300 K, and in magnetic fields up to 50 kOe. Higher temperature magnetization data were taken with a VSM (MicroSense EZ9) in the temperature range of 80–450 K and applied magnetic fields up to 20 kOe.

The electrical resistivity and magnetoresistance were measured in a PPMS. The four-probe technique was employed with a current of typically 100 μA. Measurements were made on rectangular pieces of the samples, with approximate size 5mm × 1.6mm × 0.8 mm, which were cut from the pressed pellets and polished to obtain flat surfaces. The distance between the voltage contacts is ~1 mm. The magnetoresistance was measured in the transverse configuration and is defined as the percentage change: $MR = ((\rho(H)-\rho(0))/\rho(0)) \times 100$, where $\rho(H)$ and $\rho(0)$ are the resistivity values in the presence and absence of the magnetic field, respectively.

3. Results and discussion

3.1. Structural properties

The phase formation of the pure SFMO samples at different annealing temperatures T_a from 900 °C to 1200 °C was monitored by SXRD measurements [26]. With T_a = 900 °C, the double perovskite phase forms. Besides, a significant amount of a secondary phase $SrMoO_4$ with space group $I4_1/a$ also exits. The content of the secondary phase decreases as T_a increases, and with $T_a = 1200$ °C, the sample is single-phase with the disappearance of the impurity. Further increasing T_a to 1300 °C leads to high evaporation of the gel precursor, and the sample after annealing is again multi-phase. The SXRD patterns of the SFZMO samples annealed at 1200 °C are shown in Fig. 1. For all SXRD patterns, the positions of the diffraction peaks can be well-matched with those of the standard double perovskite structure with space group $I4/m$ [40]. However, a small amount of the impurity $SrMoO_4$ still presents in the Zn doped samples. The SXRD data were refined using the Rietveld method to determine the lattice constants a and c, the microstrain ε, the average crystallite size D_{XRD}, and the molar percentage of the impurity phase. In the refinement process, the coordinates of the atoms in the main phase were applied as follows: Sr in 4d (1/2, 0, 1/4), Fe/Zn/Mo in both the B-site of 2a (0, 0, 0) and the B-site of 2b (0, 0, 1/2), and oxygen in O1 (0.289, 0.227, 0) and in O2 at (0, 0, 0.252) as in Ref. [40]. The refinement quality was checked by the goodness of fit (χ^2) and the weighted profile R-factor (R_{wp}), which approach 1 and about 10%, respectively. The values of ε and D_{XRD} were determined based on the broadening of the diffraction peaks.

The concentration of the $SrMoO_4$ phase derived from the Rietveld analysis for the SFZMO samples is in the range of 5–11 mol. %. Fig. 2 demonstrates the refinement process for the sample with $x = 0.1$ together with the experimental data. The structural parameters for the samples are listed in Table 1. The lattice constants slightly increase with

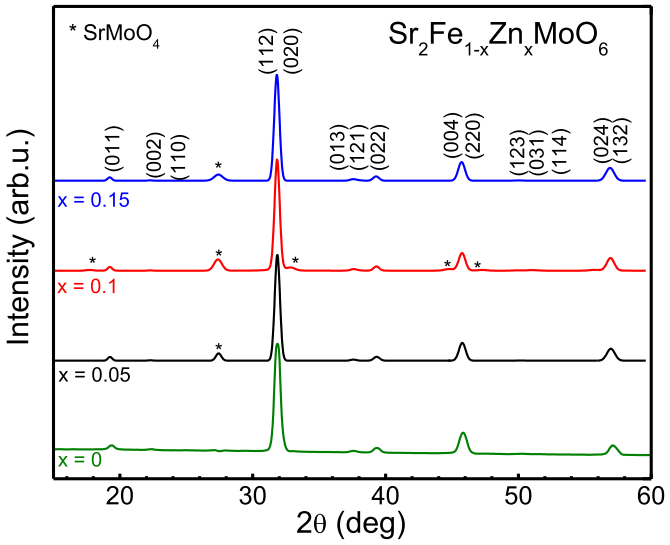

Fig. 1. SXRD patterns of the SFZMO samples with $x = 0$, 0.05, 0.1 and 0.15. The Miller indices of the Sr_2FeMoO_6 phase peaks are indicated. The peaks marked with stars are identified as those of the $SrMoO_4$ phase.

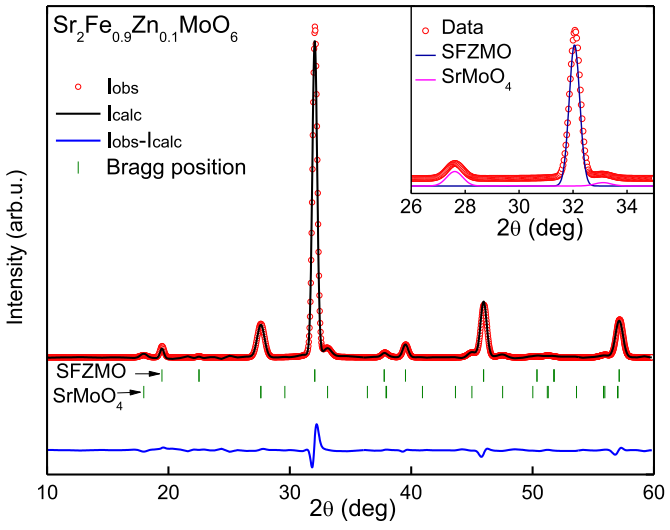

Fig. 2. Rietveld refinement of the SXRD pattern of the sample $x = 0.1$. Red circle: experiment, black line: calculation, blue line: the difference between experiment and calculation, green vertical bar: Bragg position. The inset illustrates the contributions to the intensity from $Sr_2Fe_{0.9}Zn_{0.1}MoO_6$ and $SrMoO_4$ phases in the 2θ range from 26° to 35°.

increasing Zn content from 0 to 0.15 The lattice expansion effect can be explained by the dopant Zn^{2+} ions with larger radius being located at the lattice sites ($r_{Zn2+} = 0.88$ Å, $r_{Fe3+} = 0.785$ Å, $r_{Mo5+} = 0.75$ Å, according to Ref. [41]).

According to the ICP-AES results, the molar ratio of [Sr]:[Fe]:[Zn]:[Mo] of all samples is very close to that of the nominal compositions. Hence, the concentrations of cation species in the main double perovskite phase were corrected based on the molar fraction of the $SrMoO_4$. It is seen that the actual molar fractions of Fe and Mo in the SFZMO phase change by a few percent. The chemical formula now is written as $Sr_2Fe_{1-x+y}Zn_xMo_{1-y}O_{6-y}$ with $y \leq 0.05$ as presented in Table 1.

FESEM images taken for the samples are shown in Fig. 3. It is seen from the figure that polygonal particles were formed with clear boundaries. This morphology analysis shows that via the sol-gel route, nanocrystalline structures are obtained even with the annealing temperatures as high as 1200 °C. The grain growth is inhibited by factors such as the segregation of the impurity phase $SrMoO_4$, a high-heating rate, and a short annealing time. The histograms of the lateral particle size obtained from a sampling of 300–400 particles from 4 to 5 FESEM graphs for each sample are presented in the right column of Fig. 3. The particle size data were modeled with the lognormal distribution function to estimate the average particle size D_{SEM}. The D_{SEM} values together with the standard deviation w are listed in Table 2. The average size of the particles decreases while the size distribution becomes broader with increasing the Zn content. This tendency can be due to the competition between the ion species occupying the B sites during the crystallization process. The average dimensions of the particles in the Zn doped samples are comparable to the average crystallite sizes D_{XRD} determined via the broadening of the diffraction peaks in the SXRD patterns. For the pristine compound, D_{SEM} is much larger than D_{XRD}, which indicates that the particles may contain a few crystallites.

3.2. Magnetic properties

Magnetization loops M–H were measured at different temperatures in the range between 5 and 300 K to determine the magnetic moment of the samples. The magnetization curves for the samples measured at 5 and 300 K are shown in Fig. 4. In general, the magnetization curves approach saturation at about 7 kOe. This process is a characteristic of a ferrimagnetic material, which is the case for the SFMO compound [1,4]. With further increasing the applied field, the magnetization keeps increasing in a close to the linear manner, and a fully magnetized state is not achieved at the highest applied field $H = 50$ kOe. It was shown that the bulk sample of SFMO is magnetically saturated at much lower fields, which is of the order of 1.1 kOe [42]. The magnetization process reflects the nanostructure of the samples. In the demagnetized state, the orientation of the magnetization vectors of the grains is random. Larger applied fields are thus required to overcome the effective anisotropy and magnetic interactions between neighboring grains. The observed high-field susceptibility χ_{HF} tends to be reduced with increasing the zinc

Table 1
Crystallographic and microstructural parameters of the SFZMO samples (lattice parameters a and c, unit cell volume V, average crystallite size D_{XRD}, average value of microstrain ε, degree of anti-site disorder p and cation distribution), and the fitting quality of the Rietveld refinement (χ^2 and R_{wp}).

x	0	0.05	0.1	0.15
a, Å	5.605(4)	5.607(5)	5.608(5)	5.609(6)
c, Å	7.919(5)	7.923(6)	7.923(4)	7.927(8)
V, Å^3	248.78(3)	249.08(7)	249.17(5)	249.39(3)
D_{XRD}, nm	26.0(2)	26.4(2)	34.9(3)	22.7(1)
ε, %	0.42(1)	0.51(1)	0.31(1)	0.42(1)
$SrMoO_4$, mol%	-	7 ± 0.3	11 ± 0.5	5 ± 0.3
P	0.1 ± 0.004	0.07 ± 0.004	0.09 ± 0.003	0.1 ± 0.005
Cation distribution	$[Fe_{0.9}Mo_{0.01}]_B$ $[Fe_{0.1}Mo_{0.9}]_{B'}$	$[Fe_{0.88}Zn_{0.05}Mo_{0.07}]_B$ $[Fe_{0.11}Mo_{0.89}]_{B'}$	$[Fe_{0.81}Zn_{0.1}Mo_{0.09}]_B$ $[Fe_{0.145}Mo_{0.855}]_{B'}$	$[Fe_{0.75}Zn_{0.15}Mo_{0.1}]_B$ $[Fe_{0.13}Mo_{0.87}]_{B'}$
χ^2	1.18	1.51	1.67	1.37
R_{wp}, %	8.67	11.1	10.6	10.9

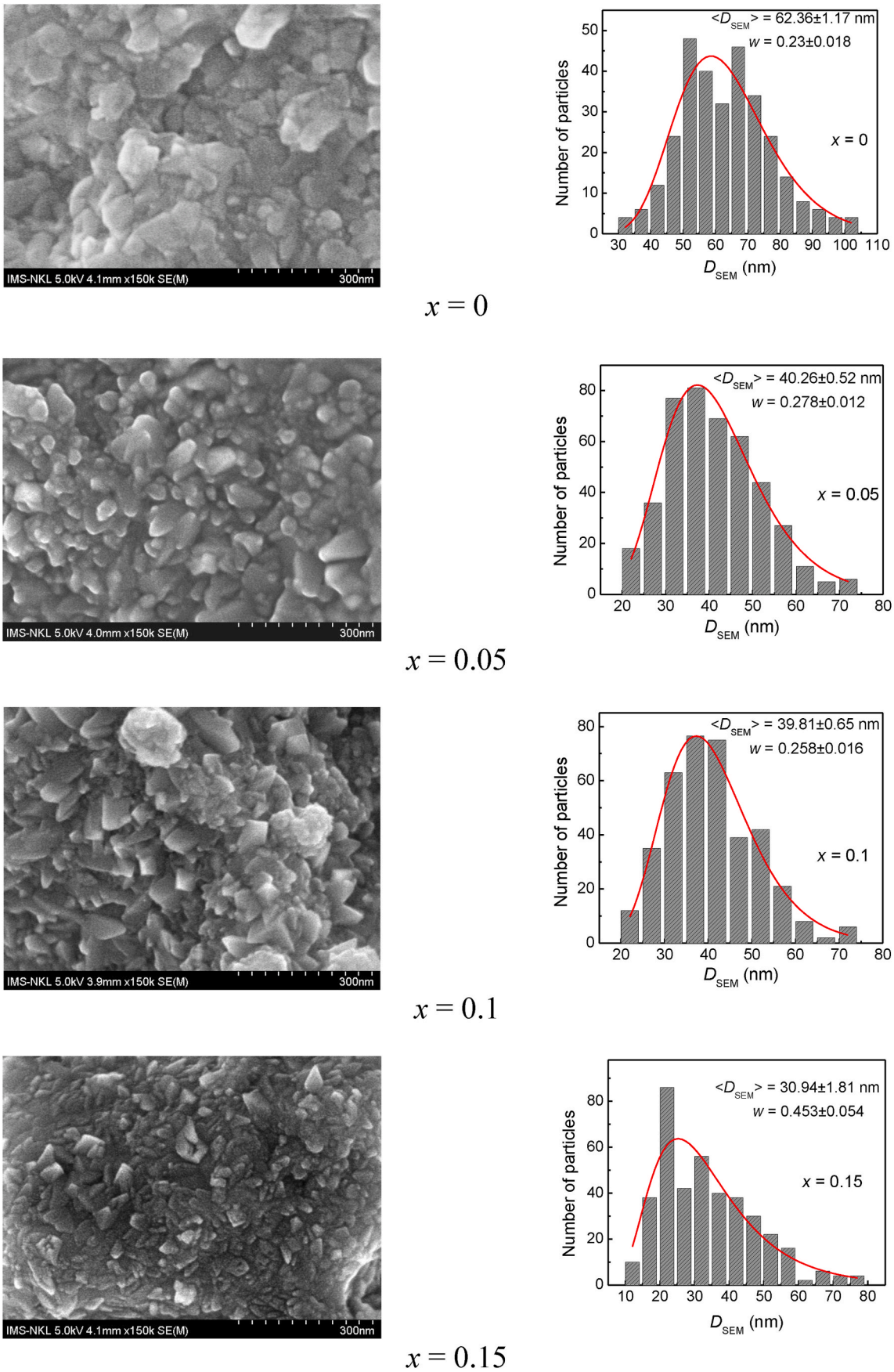

Fig. 3. (Left) SEM images of the SFZMO samples (whole scale bar 300 nm). (Right) Histograms of the particle size distribution. Red solid curves are the fit to the lognormal distribution function.

Table 2
Particle size distribution parameters D_{SEM}, w, and magnetic properties of the SFZMO samples (see text).

x	0	0.05	0.1	0.15
D_{SEM}, nm	62.3 ± 1.1	39.8 ± 0.6	40.2 ± 0.5	30.9 ± 1.8
W	0.23 ± 0.02	0.25 ± 0.01	0.27 ± 0.01	0.45 ± 0.05
M_s (5 K), emu/g	40.2	39.1	34.6	31.18
m^{exp}(5K), μ_B/f.u.	3.04	2.96	2.62	2.37
T_C, K	412	407	391	387

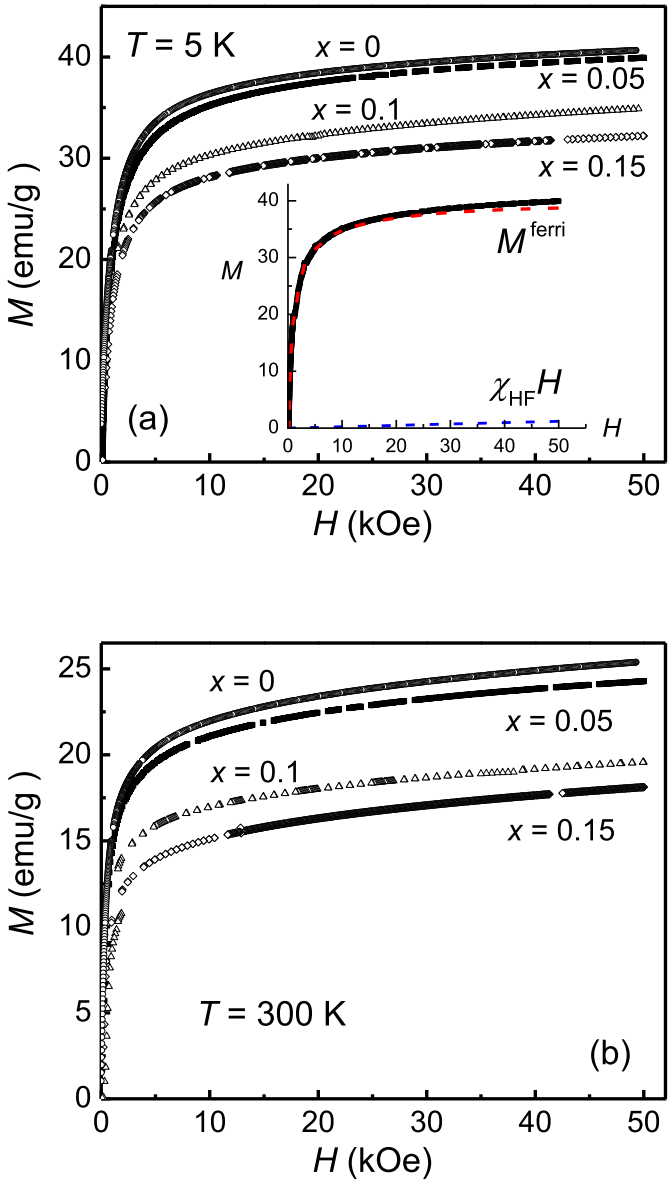

Fig. 4. Magnetization curves at (a) 5 K and (b) 300 K of the SFZMO samples. The inset of Fig. 4a shows the ferrimagnetic and spin-disorder components at 5 K for the sample $x = 0.05$, which are extracted by fitting the magnetization curve using Eq. (1).

content x. This phenomenon may have several origins. Firstly, it is attributed to antiferromagnetic Fe^{B}–O-$Fe^{B'}$ pairs created as the result of the anti-site disorder. The Fe moments in these sites are forced to align along the applied field direction when its strength increases. The magnitude of χ_{HF}, therefore, depends on the number of Fe^{B}–O-$Fe^{B'}$ pairs. As will be discussed later, this number decreases with x increasing from 0.05 to 0.15. Secondly, for the small particle systems, the spins at the interfaces are expected to be misaligned with those in the inner cores, which is another source for induced magnetization at high fields [43]. In these cases, the law of "approach to saturation" can be used to estimate the saturation magnetization M_s. The magnetization versus the magnetic field is expressed as follows [44]:

$$M = M_s\left(1 - a/H^{1/2} - b/H^2\right) + \chi_{HF}H, \quad (1)$$

where in the first term, $a/H^{1/2}$ and b/H^2 represent the influences of the defects in the lattice and the effective anisotropy, respectively, while the second term accounts for the linear contribution. To illustrate this, Fig. 4a shows the ferrimagnetic contribution and the contribution originating from the spin disorder effects, which correspond to the first and the second terms of Eq. (1), respectively. The values of the saturation magnetization M_s and corresponding saturated magnetic moment m^{exp} at 5 K are presented in Table 2. It is noted that these magnetization values of the SFZMO samples were corrected for the amounts of non-magnetic parasitic $SrMoO_4$ phase. The magnetic moment m^{exp} in Bohr magneton per formula unit was calculated from M_s in emu per gram via the relation: $m^{exp} = M_s \times$ Molmass/5585, where Molmass is the molar mass of the samples in gram. m^{exp} decreases with increasing the zinc content x, which indicates that non-magnetic Zn replaces Fe in the B sites. Similar behavior is reported in previous works for Zn doped SFMO bulks [31,36].

The saturated magnetic moment m_s of SFMO is sensitive to the anti-site disorder level p. In the simple ferrimagnetic state in which the B and B' sublattices are antiferromagnetically coupled, each Fe^{3+} ion in B' site reduces m_s by $2 \times 5\mu_B = 10\mu_B$, while each Mo^{5+} ion in a B site increases m_s by $2 \times 1\mu_B = 2\mu_B$, therefore the dependence of m_s on p can be described as $m_s = (4–8p)\mu_B$/f.u [1]. Calculated values based on this approximation are in good agreement with the experimental data [45] and Monte Carlo computation results [46]. For the SFMO sample under investigation, m_s is 3.01 μ_B/f.u., which corresponds to $p = 0.12$. The latter is close to the value derived from the Rietveld refinement (Table 1).

For zinc-doped samples, a model for the dependence of m_s upon both the anti-site disorder p and the zinc content x was proposed by Wang et al. [36]. As Zn^{2+} ions replace Fe^{3+}, Mo^{6+} ions appear according to the charge balance condition. As a consequence, non-magnetic Zn^{2+} $^{(B)}$–O–$Mo^{6+(B')}$ links form in SFZMO at the cost of the ferrimagnetic Fe^{3+} $^{(B)}$–O–$Mo^{5+(B')}$ ones. Therefore, if all Zn ions locate at the B sites, the value of m_s is given as [36]:

$$m_s = [(4 - 8p) - 4x]\mu_B/f.u., \quad (2)$$

where the second term corresponds to the decrease of the magnetic moment due to the formation of non-magnetic Zn^{2+}–O–Mo^{6+} pairs.

For the composition $Sr_2Fe_{1-x+y}Zn_xMo_{1-y}O_{6-y}$, as in the case of our samples, Eq. (2) becomes

$$m_s = [(4 - 4y - 8p) - 4x]\mu_B/f.u.. \quad (3)$$

The degree of anti-site disorder p was determined according to Eq. (3) using the m^{exp} data. The models of cation distribution for the SFZMO samples derived from this analysis are presented in Table 1. The SXRD patterns were fitted using the cation concentrations in the B and B' sites as input parameters to check the validity of these models. Good fitting results were obtained with quality parameters χ^2 and R_{wp} indicated in Table 1. For demonstration, Fig. 2 presents the Rietveld analysis data for the sample SFZMO with $x = 0.1$.

The magnetic coercivity H_c was investigated by examining the parts of the hysteresis loops around the origin (the inset of Fig. 5). In order to determine the coercivity, the loops were corrected for the demagnetization field. The effective field H_{eff} in the samples is calculated according to the relation $H_{eff} = H - 4\pi NI$, in which I is the volume magnetization in emu/cm^3 and N is the demagnetization factor (taken as 1/3 for a spherical particle). The temperature dependence of H_c is shown in Fig. 5. For the samples with $x = 0.1$ and 0.15, the coercivity becomes zero at a

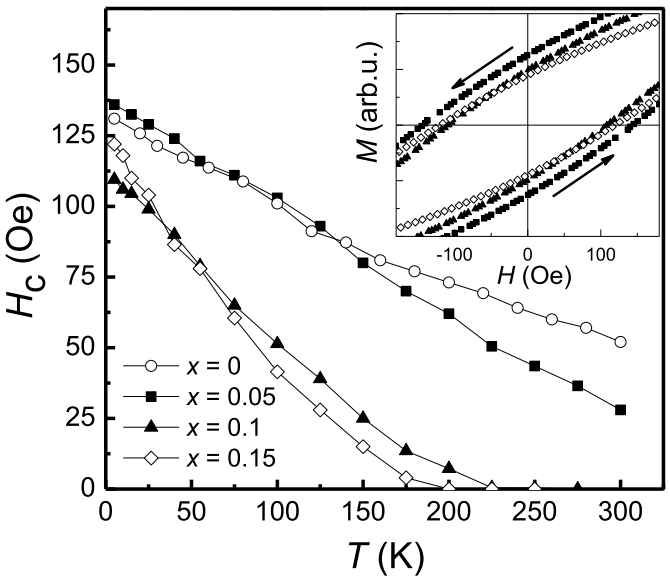

Fig. 5. Temperature dependence of the coercivity H_c of the SFZMO samples. The inset shows the magnified region of the magnetization loops at 5 K around the origin from which the coercivity was determined.

temperature well below room temperature, namely at about $T_{Hc\,=\,0}$ = 200 K and 225 K, respectively. Zero coercivity is a consequence of the influence of thermal agitation on the magnetic state in small particle systems. The magnetic anisotropy energy of a system decreases with decreasing volume. At a critical temperature, the thermal energy will overcome the effective anisotropy. Above that temperature, the sample becomes superparamagnetic. The effective anisotropy includes the magnetocrystalline anisotropy, surface and shape anisotropy, and interparticle interactions [47,48]. Superparamagnetic behavior was reported previously for SFMO nanoparticle and thin-film systems [2, 28–30]. The magnetization process of a superparamagnetic particle follows the Langevin theory as [30]:

$$M(H,T) = M_s L\left(\frac{\mu H}{k_B T}\right). \tag{4}$$

The Langevin function is

$$L\left(\frac{\mu H}{k_B T}\right) = \coth\frac{\mu H}{k_B T} - \frac{k_B T}{\mu H}, \tag{5}$$

where μ is the magnetic moment of a particle, T the temperature, H the magnetic field and k_B the Boltzmann constant. It is known that the shape of nanoparticles with sizes below ~20 nm tends to be spherical. The magnetic moment can be determined as $\mu = M_s \rho V$ where ρ is the mass density and $V = D^3/6\pi$ is the volume of the particle with diameter D_{mag}.

For particle assembly, the distribution of particle size D can generally be described by a lognormal function. This distribution has the form [49]:

$$f(D)dD = \frac{1}{\sqrt{2\pi} w D}\exp\left(-\frac{(\ln D - \ln D_0)^2}{2w^2}\right)dD, \tag{6}$$

where D_0 and w are the mean value and the standard deviation of ln$D$, respectively. The magnetization of the particle assembly in the superparamagnetic state is then expressed by Ref. [50]:

$$M(H,T) = M_s \int_0^\infty L\left(\frac{M_s \rho D_{mag}^3 H}{6\pi k_B T}\right) f(D_{mag})\, dD_{mag}. \tag{7}$$

The ferrimagnetic component M^{ferri} of the samples $x = 0.1$ and 0.15 at several temperatures above $T_{Hc\,=\,0}$ was extracted by subtracting the high-field susceptibility contribution from the total magnetization (see the inset of Fig. 4a). Plots of M^{ferri} normalized to the saturation value M_s^{ferri} as a function of H/T are shown in Fig. 6. For both samples, the curves are coinciding, which is another manifestation of superparamagnetic states. Fitting M^{ferri} to the experimental data according to Eq. (4), in which only one average value of D_{mag} is used does not give a good result. However, the data can be well fitted to Eq. (7), as demonstrated by the solid lines in Fig. 6. The best fits were obtained with the size distribution characterized by $D_0 = 11.5$ nm, $w = 0.4$ and $D_0 = 10.5$ nm, $w = 0.3$ for $x = 0.1$ and 0.15, respectively (see the insets in Fig. 6). The mean particle sizes are considerably smaller than the average crystallite sizes D_{XRD} and the lateral dimension of the particles observed via FESEM images (Fig. 4). The above analysis reveals the role of Zn and APBs in forming smaller magnetic domains in the particles. As mentioned in the introduction, the formation of Mo–O–Zn–O–Mo chains via Zn and Fe–O–Fe anti-phase boundaries divide the large ferromagnetic volumes in SFMO bulk samples into smaller ones [36]. In our samples, the ferromagnetic volumes decrease to below the

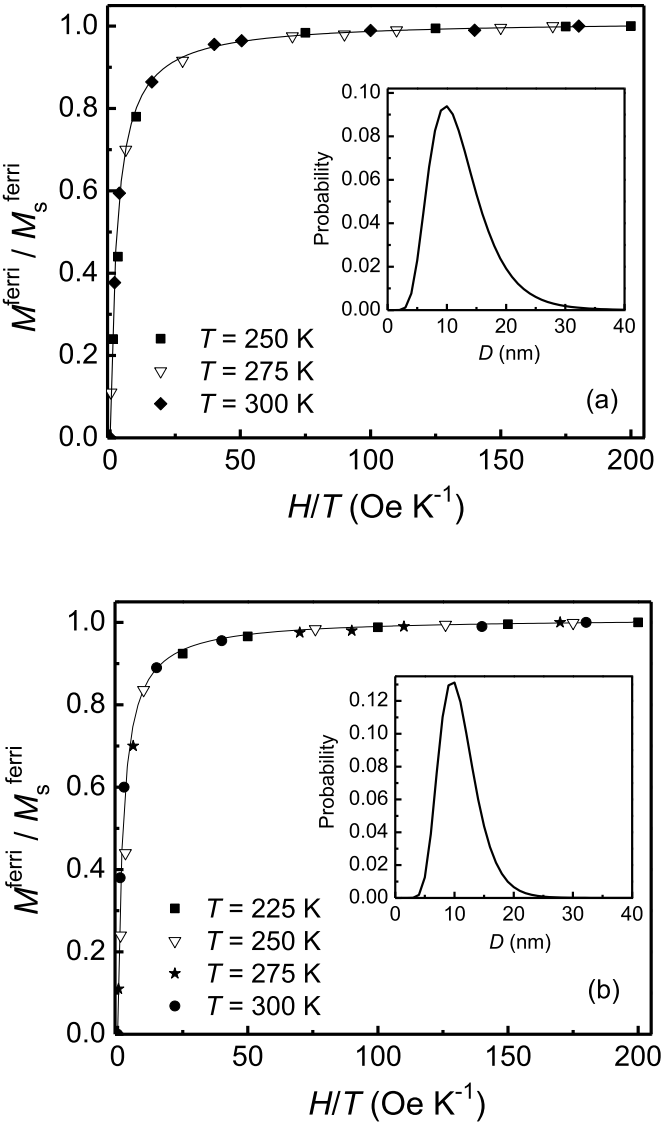

Fig. 6. Normalized ferrimagnetic magnetization M^{ferri}/M_s^{ferri} versus applied field divided by temperature H/T for the samples (a) $x = 0.1$ and (b) $x = 0.15$ at several temperatures above $T_{Hc\,=\,0}$ and in the applied field $0 \le H \le 50$ kOe. Experimental data are presented with dots, while the solid lines are fitting curves using Eq. (7). The insets show the particle size distribution derived from the fits.

superparamagnetic limit. As the density of Mo^{B}–O-$Zn^{B'}$ linkages increases with increasing the Zn concentration, the sizes of the ferromagnetic regions are smaller in the sample with higher Zn concentrations.

The magnetization versus temperature curves measured in low field $H = 100$ Oe and the high-temperature range are shown in Fig. 7, from which the magnetic phase transition is investigated. In general, the magnetization of these samples constantly decreases with increasing temperature leading to a broad transition in contrast to the sharp-drop feature observed for the bulk sample (see, e.g. Ref. [30]). This phenomenon can be explained due to the particle size distribution. As the spin coherence length becomes smaller in the small particles, the Curie temperature T_C decreases, and hence, their magnetizations drop earlier by heating the system. This effect explains a slowly decaying behavior of the total magnetization [30]. The Curie temperature was determined by the intersection between the tangential lines to the curves and the temperature axis. The magnitude of T_C depends on both the anti-site disorder and particle size. It is noted that T_C is ~420 K for the ordered SFMO bulk material [1]. The derived T_C values are listed in Table 2 and show a decreasing tendency with increasing x. In the SFZMO samples, the Mo–O–Zn–O–Mo network leads to an optimized cationic order of the Fe containing matrix phase. Based on this fact, one can conclude that the lowered T_C values compared to that of the bulk counterpart are due to the finite-size effect. According to the finite-size scaling theory, the Curie temperature of a ferromagnetic (or ferrimagnetic) material decreases with decreasing size D by the following relation [51]:

$$T_C(\infty) - T_C(D) = T_C(\infty)(\xi_0/D)^{1/\nu}, \quad (8)$$

where T_C is the bulk Curie temperature, ξ_0 is a microscopic length close to the lattice constant [52], and ν is a scaling exponent. Using the lattice constant c of about 0.79 nm for ξ_0 (Table 1) and $\nu = 0.7$ for a three-dimensional Heisenberg magnet [53], a T_C value is found to be 410 K for a particle with $D = 11$ nm according to Eq. (8). This estimated value is in good agreement with those derived for our samples.

3.2.1. Electrical transport properties

The temperature dependence of the electrical resistivity of the samples with $x = 0$, 0.05, and 0.15 was measured in a zero applied field. The resistance of the sample $x = 0.1$ is in the MΩ range. Hence, it not possible to measure the magnetoresistance effect on this sample. The resistivity values of the samples at 5 K and 300 K are shown in Table 2. At 5 K, the resistivity of the pristine compound is in the mΩcm range while it is in the Ωm range for the Zn-doped samples. The abrupt change in the resistivity of these granular systems indicates the predominant role of grain boundaries. The increase by almost five orders of magnitude is attributed to the impurity phase located at the boundaries. Also, the insulating APBs and Mo–O–Zn–O–Mo links can be additional sources of resistance. The conductance of the samples is estimated by the reciprocal of the resistance. Fig. 8 shows the temperature-dependent behavior of the conductance $\sigma(T)$, which is normalized to the value at 5 K for the samples $x = 0.05$ and 0.15. The $\sigma(T)$ curve of the pure sample $x = 0$ was reported in Ref. [16]. In all the samples, the conductance increases with increasing temperature. As seen in Fig. 8, the increase is about a factor three at 300 K. The conducting process via grain boundaries in ferromagnetic metallic systems is usually interpreted based on two mechanisms, namely the spin-dependent elastic tunneling of electrons (SDT) through the insulating barrier between adjacent grains and their high-order spin-independent inelastic hopping (SIH) through two or more localized states in the barrier [54].

The tunneling conductance σ_{SDT} depends on temperature according to the following equation [16]:

$$\sigma_{SDT} = \sigma_0\left(1 + P^2\mu^2\right)\exp\left[-(\Delta/T)^{1/2}\right], \quad (9)$$

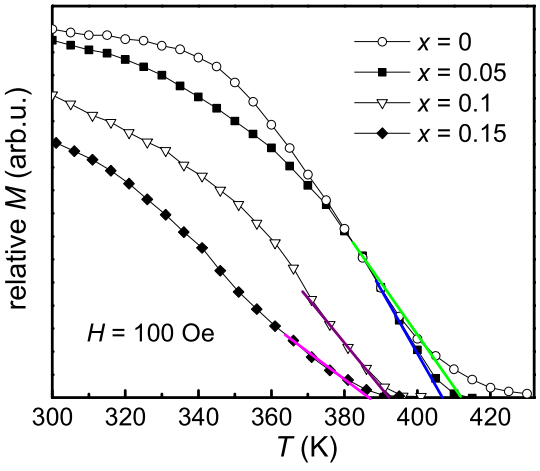

Fig. 7. Temperature dependence of relative magnetization measured in an applied field $H = 100$ Oe for the SFZMO samples.

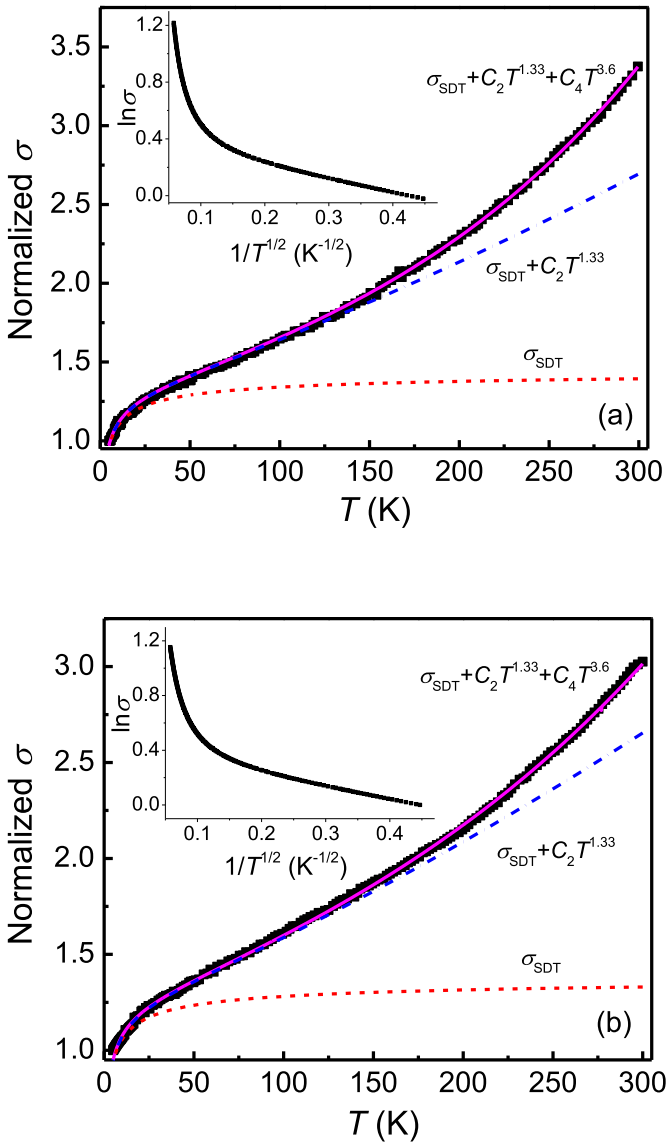

Fig. 8. Normalized conductance σ versus temperature T curves for the samples (a) $x = 0.05$ and (b) $x = 0.15$. Line curves show the fitting results and the tunneling and hopping terms according to Eq. (11). The insets show the logarithmic conductance $\ln\sigma$ as a function of $1/T^{1/2}$.

where P is the spin polarization, $\mu = M/M_s$, the relative magnetization, σ_0, a constant, and Δ is proportional to the Coulomb charging energy and thickness of the tunneling barrier. On the other hand, the hopping conductance σ_{SIH} follows a power law in temperature which is given by Ref. [54]:

$$\sigma_{SIH} \propto T^{\gamma} n, \tag{10}$$

in which $\gamma = N - [2/(N+1)]$, with N the number of localized state. In the case of second-order hopping ($N = 2$) $\gamma = 1.33$, for third-order hopping ($N = 3$) $\gamma = 2.5$, and for fourth-order hopping $\gamma = 3.6$. The total conductance is the sum of two contributions $\sigma = \sigma_{SDT} + \sigma_{SIH}$

The insets of Fig. 9 are plots of $\ln\sigma$ versus $1/T^{1/2}$. A linear behavior below about 40 K and 24 K is observed for $x = 0.05$ and 0.15, respectively. The results reveal that the conductance of the samples bears a tunneling character at low temperatures. Here it is seen that the insulating $SrMoO_4$ impurity at the grain boundaries and Mo–O–Zn–O–Mo, and Fe–O–Fe chains facilitate the electron tunneling between grains and magnetic domains. Above these temperature ranges, the curves start to deviate from linearity, indicating the rise of the high-order hopping terms. The total conductance of the samples was fitted using an expression including the tunneling term and the hopping terms up to the fourth order:

$$\sigma = C_1 \exp\left[(-\Delta/T)^{1/2}\right] + C_2 T^{1.33} + C_3 T^{2.55} + C_4 T^{3.6}. \tag{11}$$

The quantity Δ in the first term was determined from the slope of the linear parts of the $\ln\sigma$ vs. $1/T^{1/2}$ curves. The two sets of conductance data can be well reproduced without the need for the $T^{2.55}$ term. Fig. 8a and 8 b shows the theoretical results and the contributions of different terms to the total conductance of the samples. The fitting coefficients are listed in Table 3. As reported in Ref. [16], the temperature dependence of the conductance of the pure sample $x = 0$ was best described using the $T^{1.33}$ and $T^{2.55}$ terms. The increase in the order of the inelastic hopping in the Zn-doped samples indicates the changes in average barrier thickness due to impurity phases, which is associated with the increased number of localized states N.

The magnetoresistance of the three samples was measured at different temperatures from 5 K up to room temperature. Fig. 9 shows the MR curves at 5 K and 300 K, which are not saturated in applied magnetic fields up to ±50 kOe. The large negative MR values at low temperatures are consistent with the intergrain spin-dependent tunneling. At 5 K, the magnetoresistance ratio at maximum field MR_{max} reaches −28.2, −33.7% and −41.4% for the samples $x = 0$, 0.05 and 0.15, respectively. The study of Wang et al. in Ref. [36] on the magnetoresistance of the SFMO samples ($0 \leq x \leq 0.2$, step 0.05) prepared by the solid-state reaction method showed that the saturated MR value at 5 K is highest for the sample $x = 0.15$ and attains 40% in 50 kOe. The higher tunneling MR implies a better cationic order of the double perovskite phase and consequently high spin polarization.

The temperature dependence of MR_{max} of the Zn doped samples is presented in the inset of Fig. 9b. With increasing temperature, MR_{max} decreases strongly for both cases. At first, the rapid reduction in MR at high temperatures is attributed to the predominant contribution of the conductance from the spin-independent hopping channels [16,54]. In addition, the spin alignment in the particles is easier to be destroyed by thermal agitation because of the decrease of the Curie temperature in the small-size systems. This phenomenon explains the strong suppression of MR_{max} in sample $x = 0.15$ at room temperature, being lower than that of the sample $x = 0.05$ (Table 2).

The experimental magnetoresistance curves at 5 K were studied using the theory of Inoue and Maekawa for the spin-dependent elastic tunneling process as below [16]:

$$MR = -\frac{P^2\mu^2}{1 + P^2\mu^2}, \tag{12}$$

where P is the spin polarization of conduction electrons of the main phase and, μ is the reduced magnetization M/M_s. In the saturation state $\mu = 1$, hence the maximal value for tunneling MR is 50% for $P = 100\%$.

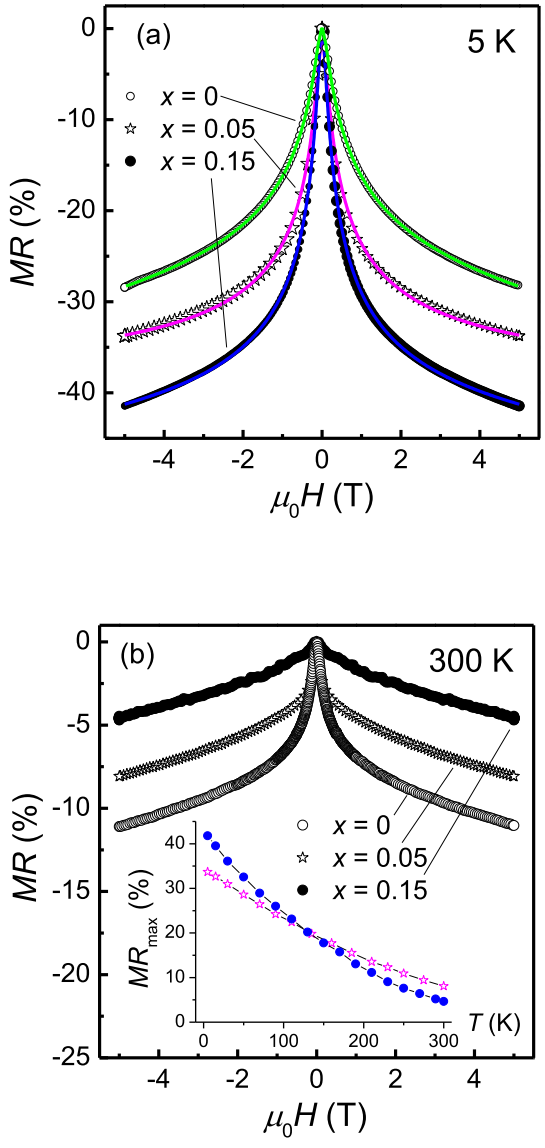

Fig. 9. Magnetoresistance MR as a function of magnetic field H for the SFZMO samples: (a) at 5 K (lines are fitting curves using Eq. (14)); and (b) at 300 K. The inset of Fig. 9b shows the temperature dependence of the MR_{max} for the two samples $x = 0.05$ and 0.15.

Table 3
Resistivity ρ, maximum resistance MR_{max}, spin polarization P at 5 K and fitting parameters for the conductance (Δ, C_1, C_2, C_4) and magnetoresistance (H_0, α) of the SFZMO samples (see text).

	0	0.05	0.15
ρ (5 K), Ωm	35×10^{-5}	11.4	9.1
MR_{max} (5 K), %	−28.2	−33.7	−41.4
P (5 K), %	74.0	88.1	99.0
Δ (K)	0.03	0.85	0.79
C_1	1.0	1.47	1.40
C_2 (10^4 $K^{-1.33}$)	0.8	6.62	6.72
C_3 (10^7 $K^{-2.55}$)	1.05	-	-
C_4 (10^{10} $K^{-3.6}$)	-	4.34	8.30
H_0 (10^2 $T^{1/2}$)	108.84	45.89	44.56
α (10^{10} T^{-1})	0.6	0.062	0.31

The highest saturated *MR* values at 5 K recorded so far are 44.2% and 46% for the undoped SFMO particulate samples with grain sizes in the range 40–80 nm by Dai et al. [55], and in the micron-scale reported by Harnagea et al. [56], respectively. For the latter, an estimation from Eq. (12) gives a spin polarization value $P = 92\%$. From its saturation magnetic moment at 5 K of 3.6 μ_B/f.u. [56], the degree of anti-site disorder is approximately equal to five percent according to the relation $m_s = (4–8p)\mu_B$. For our samples, the MR_{max} does not yet reach a saturated value. Fitting the experimental *MR* curves based on Eq. (12) using the field dependence of the magnetization as shown in Fig. 4 was unsuccessful. A previous study showed that tunneling processes between magnetic particles rely on the orientation of the spins in the vicinity of the grain boundaries [57]. In the nanoparticles, the spins in the outer layer usually deflect from the inner spin direction because of symmetry breaking of atomic coordination and interactions with the surface spins in the adjacent particles. Therefore, near the grain boundaries, the spins can be frozen randomly. In this case, the expression for the magnetization process $\mu(H)$ of spin-glass systems can be used [57]:

$$\mu(H) = \exp\left(-H_0 \Big/ \sqrt{H}\right). \quad (13)$$

Excellent fits to the *MR* data of our samples were obtained using a modified form of Eq. (12):

$$MR = -\frac{P^2\mu^2}{1+P^2\mu^2} - \alpha H, \quad (14)$$

in which μ is described by Eq. (13), and the linear term $-\alpha H$ is added to account for a small contribution from other possible spin disorder sources in the samples. The fitting curves are shown in Fig. 9, and the fitting parameters are listed in Table 3. For the pure SFMO sample, *P* attains 74% at 5 K. Remarkably, very high spin polarization values were deduced for the samples with $x = 0.05$ and $x = 0.15$, namely $P = 88.1\%$ and 99%, respectively. The much-improved degree of spin polarization in the SFZMO samples supports the morphological and magnetic studies in the preceding sections. These results confirm that the crystal structure in the magnetic domains becomes perfect due to the segregation of the insulating networks formed by the Mo^B–O-$Zn^{B'}$ linkages and APBs [27, 36].

4. Conclusions

In summary, nano-sized SFZMO samples were synthesized using the sol-gel route with a short annealing time. The influence of the site occupancy of doping Zn and anti-site disorder on the magnetic and magnetotransport properties was clarified. The Zn^{2+} ions do not distribute evenly in the lattice but form Mo^B–O–$Zn^{B'}$-O-Mo^B networks, which divide the particle volumes into small ferromagnetic domains with a high degree of Fe/Mo order. These domains in the samples with $x = 0.1$ and 0.15 are superparamagnetic below room temperature. This study confirms that highly ordered SFZMO can be obtained based on the crystallographic site preference of Zn atoms. With this structural characteristic, the spin polarization of nearly 100% is achieved in the sample with $x = 0.15$.

Funding

This study was funded by the Vietnam National Foundation for Science and Technology Development (Grant No. 103.02–2019.321).

Declaration of competing interest

The authors declare that they have no known competing financial interests or personal relationships that could have appeared to influence the work reported in this paper.

Acknowledgment

This work was financially supported by the Vietnam National Foundation for Science and Technology Development under Grant No. 103.02-2019.321.

References

[1] D. Serrate, J.M. De Teresa, M.R. Ibarra, Double perovskites with ferromagnetism above room temperature, J. Phys. Condens. Matter 19 (2007), 023201.
[2] F. Mezzadri, D. Delmonte, F. Orlandi, C. Pernechele, G. Calestani, M. Solzi, M. Lantieri, G. Spina, R. Cabassi, F. Bolzoni, M. Fittipaldi, M. Merlini, A. Migliori, P. Manuel, E. Gilioli, Structural and magnetic characterization of the double perovskite Pb_2FeMoO_6, J. Mater. Chem. C 4 (2016) 1533–1542.
[3] P. Chen, B.-G. Liu, Giant ferroelectric polarization and electric reversal of strong spontaneous magnetization in multiferroic Bi_2FeMoO_6, J. Magn. Magn Mater. 441 (2017) 497–502.
[4] K.I. Kobayashi, T. Kimura, H. Sawada, K. Terakura, Y. Tokura, Room-temperature magnetoresistance in an oxide material with an ordered double-perovskite structure, Nature 395 (1998) 677.
[5] C.L. Yuan, S.G. Wang, W.H. Song, T. Yu, J.M. Dai, S.L. Ye, Y.P. Sun, Enhanced intergrain tunneling magnetoresistance in double perovskite Sr_2FeMoO_6 polycrystals with nanometer-scale particles, Appl. Phys. Lett. 75 (1999) 3853.
[6] T.H. Kim, M. Uehara, S.-W. Cheong, S. Lee, Large room-temperature intergrain magnetoresistance in double perovskite $SrFe_{1-x}$(Mo or Re)$_xO_3$, Appl. Phys. Lett. 74 (1999) 1737.
[7] D.D. Sarma, S. Ray, K. Tanaka, M. Kobayashi, A. Fujimori, P. Sanyal, H. R. Krishnamurthy, C. Dasgupta, Intergranular magnetoresistance in Sr_2FeMoO_6 from a magnetic tunnel barrier mechanism across grain boundaries, Phys. Rev. Lett. 98 (2007) 157205.
[8] Y. Hu, T. Guo, X. Wang, Y. Cui, W. Li, X. Zhao, H. Liu, Magnetocaloric properties of the A-site co-doping double-perovskite of Sr_2FeMoO_6, J. Magn. Magn Mater. (2018), https://doi.org/10.1016/j.jmmm.2018.07.001.
[9] Y. Hu, X. Zhao, X. Wang, S. Wang, Effects of Nd doping on the magnetocaloric properties of double perovskite Sr_2FeMoO_6, J. Magn. Magn Mater. (2019), https://doi.org/10.1016/j.jmmm.2019.166212.
[10] I. Hussain, M.S. Anwar, S.N. Khan, A. Shahee, Z.U. Rehman, B.H. Koo, Magnetocaloric effect and magnetic properties of the isovalent Sr^{2+} substituted Ba_2FeMoO_6 double perovskite, Ceram. Int. (2017), https://doi.org/10.1016/j.ceramint.2017.05.027.
[11] G. Song, W. Zhang, Comparative studies on the room-temperature ferrielectric and ferrimagnetic Ni_3TeO_6-type A_2FeMoO_6 compounds (A = Sc, Lu), Sci. Rep. 6 (2016) 20133.
[12] S. Ravi, C. Senthilkumar, Multiferroism in new Bi_2FeMoO_6 material, Mater. Express 5 (2015) 68–72.
[13] J. Navarro, J. Nogués, J.S. Muñoz, J. Fontcuberta, Antisites and electron-doping effects on the magnetic transition of Sr_2FeMoO_6 double perovskite, Phys. Rev. B 67 (2003) 174416.
[14] O.N. Meetei, O. Erten, A. Mukherjee, M. Randeria, N. Trivedi, P. Woodward, Theory of half-metallic double perovskites. I. Double exchange mechanism, Phys. Rev. B 87 (2013) 165104.
[15] M. Bibes, K. Bouzehouane, A. Barthélémy, M. Besse, Tunnel magnetoresistance in nanojunctions based on Sr_2FeMoO_6, Appl. Phys. Lett. 83 (2003) 2629.
[16] L.D. Hien, N.P. Duong, L.N. Anh, T.T. Loan, S. Soontaranon, A. de Visser, Correlations between structural, magnetic and electronic transport properties of nano-sized (Sr,La)-(Fe,Mo) double perovskites, J. Alloys Compd. 793 (2019) 375–384.
[17] S. Ray, A. Kumar, D.D. Sarma, R. Cimino, S. Turchini, S. Zennaro, N. Zema, Electronic and magnetic structures of Sr_2FeMoO_6, Phys. Rev. Lett. 87 (2001), 097204.
[18] Y. Tomioka, T. Okuda, Y. Okimoto, R. Kumai, K.I. Kobayashi, Magnetic and electronic properties of a single crystal of ordered double perovskite Sr_2FeMoO_6, Phys. Rev. B 61 (2000) 422.
[19] H. Yanagihara, Wesley Cheong, M.B. Salamon, Sh Xu, Y. Moritomo, Critical behavior of single-crystal double perovskite Sr_2FeMoO_6, Phys. Rev. B 65 (2002), 092411.
[20] O. Chmaissem, R. Kruk, B. Dabrowski, D.E. Brown, X. Xiong, S. Kolesnik, J. D. Jorgensen, C.W. Kimball, Structural phase transition and the electronic and magnetic properties of Sr_2FeMoO_6, Phys. Rev. B 62 (2000) 14197.
[21] J.-S. Kang, J.H. Kim, A. Sekiyama, S. Kasai, S. Suga, S.W. Han, K.H. Kim, T. Muro, Y. Saitoh, C. Hwang, C.G. Olson, B.J. Park, B.W. Lee, J.H. Shim, J.H. Park, B.I. Min, Bulk-sensitive photoemission spectroscopy of A_2FeMoO_6 double perovskites (A = Sr, Ba), Phys. Rev. B 66 (2002) 113105.
[22] C. Du, R. Adur, H. Wang, A.J. Hauser, F. Yang, P.C. Hammel, Control of magnetocrystalline anisotropy by epitaxial strain in double perovskite Sr_2FeMoO_6 films, Phys. Rev. Lett. 110 (2013) 147204.
[23] A.J. Hauser, R.E.A. Williams, R.A. Ricciardo, A. Genc, M. Dixit, J.M. Lucy, P. M. Woodward, H.L. Fraser, F. Yang, Unlocking the potential of half-metallic Sr_2FeMoO_6 films through controlled stoichiometry and double-perovskite ordering, Phys. Rev. B 83 (2011), 014407.
[24] Y.H. Huang, M. Karppinen, H. Yamauchi, J.B. Goodenough, Systematic studies on effects of cationic ordering on structural and magnetic properties in Sr_2FeMoO_6, Phys. Rev. B 73 (2006) 104408.

[25] C.L. Yuan, S.G. Wang, W.H. Song, T. Yu, J.M. Dai, S.L. Ye, Y.P. Sun, Enhanced intergrain tunneling magnetoresistance in double perovskite Sr_2FeMoO_6 polycrystals with nanometer-scale particles, Appl. Phys. Lett. 75 (1999) 3853.

[26] L.D. Hien, N.P. Duong, L.N. Anh, D.T.T. Nguyet, T.T. Loan, S. Soontaranon, W. Klysubun, T.D. Hien, Tailoring magnetoresistance in nanosized Sr_2FeMoO_6 by varying the content of the parasitic $SrMoO_4$ phase, Sci. Adv. Mater. 10 (2018) 1258–1267.

[27] C. Meneghini, S. Ray, F. Liscio, F. Bardelli, S. Mobilio, D.D. Sarma, Nature of "Disorder'' in the ordered double perovskite Sr_2FeMoO_6, Phys. Rev. Lett. 103 (2009), 046403.

[28] N.A. Kalanda, S.E. Demyanov, A.V. Petrov, D.V. Karpinsky, M.V. Yarmolich, S. K. Oh, S.C. Yu, D.-H. Kim, Interrelation between the structural, magnetic and magnetoresistive properties of double-perovskite $Sr_2FeMoO_{6-\delta}$ thin films, J. Electron. Mater. 45 (2016) 3466–3472.

[29] A. Poddar, R.N. Bhowmik, I.P. Muthuselvam, N. Das, Evidence of disorder induced magnetic spin glass phase in Sr_2FeMoO_6 double perovskite, J. Appl. Phys. 106 (2009), 073908.

[30] T. Suominen, J. Raittila, T. Salminen, K. Schlesier, J. Lindén, P. Paturi, Magnetic properties of fine SFMO particles: Superparamagnetism, J. Magn. Magn Mater. 309 (2007) 278–284.

[31] F. Sriti, A. Maignan, C. Martin, B. Raveau, Influence of Fe-site substitutions upon intragrain and intergrain magnetoresistance in the double-perovskite Ba_2FeMoO_6, Chem. Mater. 13 (2001) 1746–1751.

[32] X.M. Feng, G. H Rao, G. Y Liu, H.F. Yang, W.F. Liu, Z.W. Ouyang, L.T. Yang, Z. X Liu, R.C. Yu, C.Q. Jin, J. K Liang, Structure and magnetoresistance of the double perovskite Sr_2FeMoO_6 doped at the Fe site, J. Phys. Condens. Matter 14 (2002) 12503–12511.

[33] C. Li, Y. Cailei, X. Junmin, J. Wang, Enhancement of magnetization and Curie temperature in Sr_2FeMoO_6 by Ni doping, J. Am. Ceram. Soc. 89 (2006) 672–674.

[34] L. Chen, C. Yuan, J. Xue, J. Wang, B-site ordering and magnetic behaviours in Ni-doped double perovskite Sr_2FeMoO_6, J. Phys. D Appl. Phys. 38 (2005) 4003–4008.

[35] F. Sher, A. Venimadhav, M.G. Blamire, B. Dabrowski, S. Kolesnik, J.P. Attfield, Structural, magnetic and transport properties of $Sr_2Fe_{1-x}Mg_xMoO_6$ $(0 \leq x \leq 1)$ double perovskites, Solid State Sci. 7 (2005) 912–919.

[36] X. Wang, Y. Sui, Q. Yang, J. Cheng, Z. Qian, Z. Liu, W. Su, Effect of doping Zn on the magnetoresistance of polycrystalline Sr_2FeMoO_6, J. Alloys Compd. 431 (2007) 6–9.

[37] M.F. Lü, J.P. Wang, J.F. Liu, W. Song, X.F. Hao, D.F. Zhou, X.J. Liu, Z.J. Wu, J. Meng, An investigation of low-field magnetoresistance in the double perovskites $Sr_2Fe_{1-x}Zn_xMoO_6$, $x = 0$, 0.05, 0.15 and 0.25, J. Phys. Condens. Matter 18 (2006) 1601–1612.

[38] J. Rodríguez-Carvajal, Recent advances in magnetic structure determination by neutron powder diffraction, Phys. B Condens. Matter 192 (1993) 55.

[39] L.B. McCusker, R.B. Von Dreele, D.E. Cox, D. Louër, P. Scardi, Rietveld refinement guidelines, J. Appl. Crystallogr. 32 (1999) 36.

[40] O. Chmaissem, R. Kruk, B. Dabrowski, D.E. Brown, X. Xiong, S. Kolesnik, J. D. Jorgensen, C.W. Kimball, Structural phase transition and the electronic and magnetic properties of Sr_2FeMoO_6, Phys. Rev. B 62 (2000) 14197.

[41] R.D. Shannon, Revised effective ionic radii and systematic studies of interatomic distances in halides and chalcogenides, Acta Crystallogr. A 32 (1976) 751.

[42] J. Navarro, Ll Balcells, F. Sandiumenge, M. Bibes, A. Roig, B. Martínez, J. Fontcuberta, Antisite defects and magnetoresistance in Sr_2FeMoO_6 double perovskite, J. Phys. Condens. Matter 13 (2001) 8481–8488.

[43] R.H. Kodama, A.E. Berkowitz, E.J. McNiff Jr., S. Foner, Surface spin disorder in $NiFe_2O_4$ nanoparticles, Phys. Rev. Lett. 77 (1996) 394.

[44] Z.-Q. Jin, W. Tang, J.-R. Zhang, H.-X. Qin, Y.-W. Du, Effective magnetic anisotropy of nanocrystalline Nd-Fe-Ti-N hard magnetic alloys, Eur. Phys. J. B 3 (1998) 41–44.

[45] Y. Moritomo, N. Shimamoto, S. Xu, A. Machida, E. Nishibori, M. Takata, M. Sakata, A. Nakamura, Effects of *B*-site disorder in Sr_2FeMoO_6 with double perovskite structure, Jpn. J. Appl. Phys. 40 (2001) L672.

[46] A.S. Ogale, S.B. Ogale, R. Ramesh, T. Venkatesan, Octahedral cation site disorder effects on magnetization in double-perovskite Sr_2FeMoO_6: Monte Carlo simulation study, Appl. Phys. Lett. 75 (1999) 537–539.

[47] N.T. Lan, N.P. Duong, T.D. Hien, Influences of cobalt substitution and size effects on magnetic properties of coprecipitated Co–Fe ferrite nanoparticles, J. Alloys Compd. 509 (2011) 5919–5925.

[48] L.N. Anh, T.T. Loan, N.P. Duong, S. Soontaranon, T.T.V. Nga, T.D. Hien, Influence of Y and La substitution on particle size, structural and magnetic properties of nanosized nickel ferrite prepared by using citrate precursor method, J. Alloys Compd. 647 (2015) 419–426.

[49] M. Blanco-Mantecón, K. O'Grady, Grain size and blocking distributions in fine particle iron oxide nanoparticles, J. Magn. Magn Mater. 203 (1999) 50–53.

[50] A. Tamion, M. Hillenkamp, F. Tournus, E. Bonet, V. Dupuis, Accurate determination of the magnetic anisotropy in cluster-assembled nanostructures, Appl. Phys. Lett. 95 (2009), 062503.

[51] J. Wang, F. Zhao, W. Wu, G.-M. Zhao, Finite-size scaling relation of the Curie temperature in barium hexaferrite platelets, J. Appl. Phys. 110 (2011) 123909.

[52] M.E. Fisher, M.N. Barber, Scaling theory for finite-size effects in the critical region, Phys. Rev. Lett. 28 (1972) 1516.

[53] K. Chen, A.M. Ferrenberg, D.P. Landau, Static critical behavior of three-dimensional classical Heisenberg models: a high-resolution Monte Carlo study, Phys. Rev. B 48 (1993) 3249.

[54] J. Dai, J. Tang, Temperature dependence of the conductance and magnetoresistance of CrO_2 powder compacts, Phys. Rev. B 63 (2001), 064410.

[55] J.M. Dai, W.H. Song, S.G. Wang, S.L. Ye, K.Y. Wang, J.J. Du, Y.P. Sun, J. Fang, J. L. Chen, B.J. Gao, Ordered double-perovskite Ca_2FeMoO_6 compounds with nanometer-scale grains: structure, magnetism, and intergrain tunneling magnetoresistance, Mater. Sci. Eng. B 83 (2001) 217–222.

[56] L. Harnagea, B. Jurca, P. Berthet, Low-field magnetoresistance up to 400K in double perovskite Sr_2FeMoO_6 synthesized by a citrate route, J. Solid State Chem. 211 (2014) 219–226.

[57] D. Serrate, J.M. De Teresa, P.A. Algarabel, M.R. Ibarra, J. Galibert, Intergrain magnetoresistance up to 50 T in the half-metallic $(Ba_{0.8}Sr_{0.2})_2FeMoO_6$ double perovskite: spin-glass behavior of the grain boundary, Phys. Rev. B 71 (2005) 1.